communications earth & environment

Article

https://doi.org/10.1038/s43247-024-01631-0

Translithospheric magma plumbing system fossilized in the Emeishan large igneous province

Sixue Wang[1,2], Hao Liu[1,2], Yong Zheng[1,2] ✉, Yun Chen[3,4] ✉, Sanxi Ai[1,2], Sijia Zeng[1,2], Lei Qin[1,2], Rumeng Guo[5], Xiaohui Yuan[6] & Yi-Gang Xu[7]

Lighting up the magma plumbing system beneath a large igneous province (LIP) is challenging because the complex magma migration paths are often covered by flood basalts and sediments. Here, we present a three-dimensional seismic image of the Permian Emeishan LIP in Southwest China, constructed by joint inversion of Rayleigh wave dispersions and receiver functions. The results outline a cylindrical, high-velocity anomaly extending to ~135 km depth below the inner zone of this continental LIP. The geometry and magnitude of the high-velocity anomaly suggest that it represents culminated crystallized materials of primary magmas, thereby mirroring a magma plumbing system fossilized in the lithosphere. Furthermore, our geodynamic models illustrate that the nearly vertical plumbing system was controlled by slow plate motion during the magma emplacement. The plume head beneath a nearly static plate has higher thermal buoyancy and thus promotes more intensive magma emplacement. This phenomenon may apply to other LIPs throughout Earth's history

The magma plumbing system within a large igneous province (LIP) is controlled by the plume activity, which can transport materials and heat from the core-mantle boundary to the surface[1–3]. Investigating the magma plumbing system offers key insights into the interactions of the plume with ambient mantle, mantle convection, plate tectonics and surface processes[4–6]. Nonetheless, the deep structure of large igneous provinces remains poorly characterized by geochemical and petrological approaches because much of the magma is concealed beneath the thick flood basalts and sediments. Seismic tomography could allow deep mantle plumes to be imaged; however, it is hard to isolate the thermal effects of modern plumes from compositional changes, which may lead to erroneous estimates of geometry and compositional features of plumes[7]. Thus, the dynamics of mantle plumes and their relation to mantle convection and plate tectonics are still debated. Fortunately, the continental lithosphere could preserve the imprints of an ancient LIP in fossil form[8], and allows the geometry of entire plumbing systems to be reconstructed by geophysical properties.

The Emeishan LIP (Fig. 1a), Southwest China, is a type example of continental flood basalt provinces that has been widely attributed to the activity of an ancient mantle plume in the Permian[4,9,10]. Its thermal effects caused by the plume have decayed out[11], thus providing an exceptional region for investigating the nature of LIPs' magma plumbing systems. This province encompasses vast quantities of continental flood basalts, rare picrite and associated mafic-ultramafic intrusions[4,12,13], covering a rhombus-shaped area of more than 250,000 km^2 in the western Yangtze Craton (Fig. 1a). These extensive mafic volcanic successions were emplaced over the Middle-Late Permian boundary (~260 Ma)[4,14], coeval with the end-Guadalupian mass extinction[15,16]. According to the extent of erosion of the Maokou Formation, which is unconformably overlain by the Permian flood basalt, the Emeishan LIP is divided into the inner (INZ), intermediate (IMZ), and outer (OTZ) zones[10]. Specifically, the INZ, where the erosion of the Maokou formation is most intensive and the pre-eruptive domal uplift is estimated to be the highest over 1000 m with a radius exceeding 700 km, is considered to be the impact site of the Permian plume head[4,10].

Numerous geophysical studies found evidence for large-volume magma reservoirs preserved as thick high-seismic-velocity layers (>10 km) attached to the base of the LIP's crust, such as the Deccan, Siberian

[1]Hubei Subsurface Multi-scale Imaging Key Laboratory, School of Geophysics and Geomatics, China University of Geosciences, Wuhan, 430074, China. [2]State Key Laboratory of Geological Processes and Mineral Resources, School of Geophysics and Geomatics, China University of Geosciences, Wuhan, 430074, China. [3]State Key Laboratory of Lithospheric Evolution, Institute of Geology and Geophysics, Chinese Academy of Sciences, Beijing, 100029, China. [4]Innovation Academy for Earth Science, Chinese Academy of Sciences, Beijing, 100029, China. [5]State Key Laboratory of Geodesy and Earth's Dynamic, Innovation Academy for Precision Measurement Science and Technology, Chinese Academy of Sciences, Wuhan, 430077, China. [6]Deutsches GeoForschungsZentrum GFZ, Potsdam, 14473, Germany. [7]State Key Laboratory of Isotope Geochemistry, Guangzhou Institute of Geochemistry, Chinese Academy of Sciences, Guangzhou, 510640, China. ✉e-mail: zhengyong@cug.edu.cn; yunchen@mail.iggcas.ac.cn

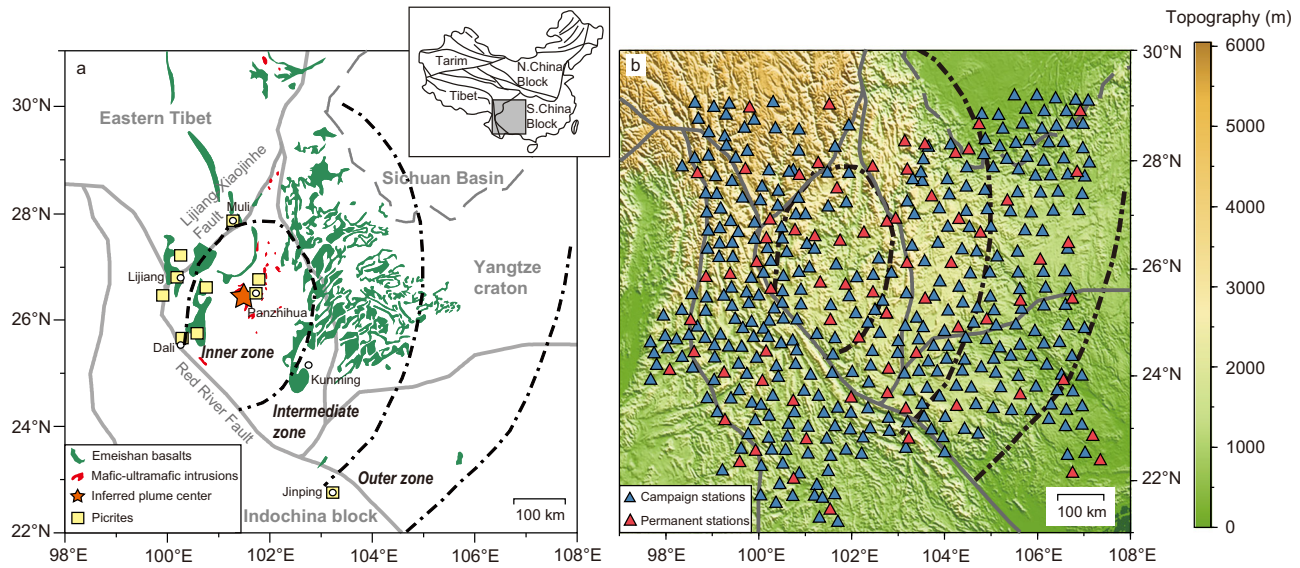

Fig. 1 | Maps of the Emeishan large igneous province (LIP) and seismic network. **a** The gray thick lines indicate the block boundaries and main faults. The gray dashed line indicates the border of the Sichuan Basin. The black dashed lines indicate the borders of the inner, intermediate, and outer zones of the Emeishan LIP. The green and red areas indicate the distribution of the Permian basalts and mafic-ultramafic intrusions, respectively[13]. The yellow squares indicate the location of the picrites[12]. The orange star indicates the inferred plume center in this study, which is also shown in Fig. 4. **b** The campaign stations deployed by ChinArray project and permanent stations deployed by the China Earthquake Administration are labeled in blue and red, respectively.

Tarps, Ontong Java Plateau, Kerguelen, Columbia River Basalts and High Arctic LIP[17–19]. However, so far, a comprehensive picture of the magma plumbing system fossilized in a LIP has not been achieved. Here, we provide a panoptic view of the Permian magma plumbing system rooted in the lithosphere by building three-dimensional (3-D) tomographic images of the crust and upper mantle beneath the Emeishan LIP. We then integrate constraints from geophysics, geochemistry, and geodynamic models to ascertain the slow motion of the overlying plate in favor of a rapid and vertical migrating magmatism of the Emeishan LIP. The results shed light on how the mantle plume interacts with the overlying lithosphere and what controls the fast magma transport and eruption of massive flood basalts.

Results

Between August 2011 and August 2013, 350 campaign stations from the ChinArray project[20] were deployed in the vicinity of the Emeishan LIP. Integrated with 74 permanent stations operated by the China Earthquake Administration[21], a substantial seismic dataset was collected using a dense seismic array featured by an inter-station spacing of ~30 km (Fig. 1b). Based on this seismic dataset, we adopt a wave gradiometry method[22–24], taking advantage of wavefield information sampled by dense arrays, to extract dispersion curve beneath each station for a period range of 20–150 s (Supplementary Fig. 1), which are sensitive to the crust and upper mantle structures. 146 teleseismic events (Mw > 5.0) with epicentral distances ranging from 30° to 90° (Supplementary Fig. 2) are used to extract these dispersion curves. Additionally, a seismic model of China[25,26] (0.5° × 0.5° grids) provides dispersion curves for shorter periods (5–40 s), mostly sensitive to the crustal structure. Differences between these two types of dispersions at overlapping periods (20–40 s) generally follow a Gaussian distribution (Supplementary Fig. 3) with small mean values (0.003–0.01 km s^{-1}) and standard deviations (0.0639-0.0753 km s^{-1}), indicating that the dispersion data from the two methods are in good consistency. Combining these two types of dispersions and using their mean values at overlapping periods, the final period range of our dispersion curves expands to 5–150 s, which provides reliable constraints on the shear wave velocity model of the crust and upper mantle. The substantial seismic dataset is also used to calculate receiver functions at each station by time-domain iterative deconvolution technique[27,28]. The harmonic stripping method[29] is used to extract the average receiver function (9 s after the direct P-wave arrival) for each station (see "Methods" section for details).

We employ a Bayesian Monte Carlo approach for joint inversion of dispersion curves and receiver functions to construct the 1-D shear-wave velocity (Vs) model beneath each station[29]. Parameterization and associated uncertainties are described in detail in the Methods section. Supplementary Fig. 4 exhibits three depth-dependent models located in the INZ, IMZ, and OTZ of the Emeishan LIP, respectively, showing that the phase velocities, receiver functions and shear wave velocities are all fitted well in the joint inversion. The 1-D Vs models at all stations are assembled to construct the final 3-D seismic model in and around the Emeishan LIP, which has a high lateral resolution of ~30 km (theoretically estimated by the station interval). Overall, velocity uncertainties are ~0.06 km s^{-1} in the crust and ~0.1 km s^{-1} in the lithospheric mantle (Supplementary Fig. 5), which are both acceptable.

Our seismic model reveals an obvious high-velocity-anomaly (HVA) with various geometric distributions and magnitudes of velocity anomaly at different depths (Fig. 2), which is well-confined to the INZ and extends to ~135 km depth (Fig. 3d, h). This translithospheric HVA is characterized by large magnitude of high velocities (Vs anomaly > 4%) in three sectors: (1) The first sector is at depths shallower than ~20 km (Fig. 2a, b; sector A in Fig. 4). The HVA extends northeastwards from the INZ to OTZ in this sector, with a lateral extent of approximately 185 km in the east-west direction and over 300 km in the north-south direction. The spatial extent of this anomaly is well constrained within the INZ, but it is less well constrained to the northeast because of the lack of seismic stations in that area. (2) The second sector is at depth range of ~40–60 km (Fig. 2d; sector C in Fig. 4), where the HVA is around 15 km thick and 210 km in diameter, which attaches to the crustal basement; (3) In the third sector, at depths of ~100–135 km (Fig. 2g; sector E in Fig. 4), the HVA is observed as a cylinder with a diameter of ~125 km. The HVA is also featured by moderate magnitude high velocities (Vs anomaly of ~3%) at depths of ~30–40 km (Fig. 2c; sector B in Fig. 4) and ~60–100 km (Fig. 2e, f; sector D in Fig. 4), whose lateral extent is ~80 km and ~100 km, respectively. Overall, the HVA forms a clear quasi-cylinder extending from the surface to the depth of at least

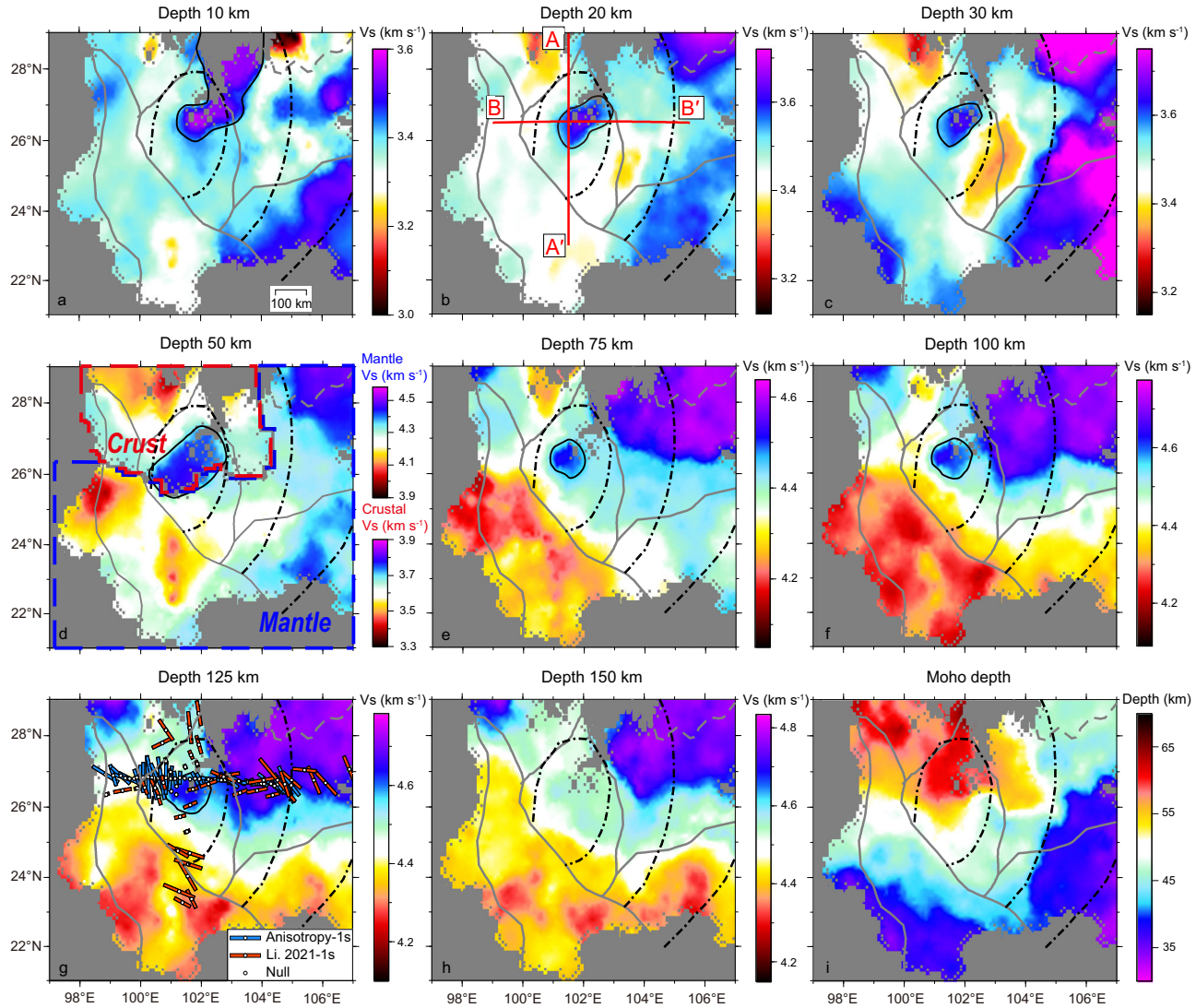

Fig. 2 | Horizontal images of tomographic inversion for S-wave velocity structure and the Moho depth. Colour scale denotes the magnitude of S-wave velocity at 10–150 km depths (**a**–**h**) and the depth of Moho discontinuity (**i**). The gray and black lines are the same as those in Fig. 1a. Black circles indicate the maximum gradient of velocity perturbations around the high-velocity anomaly in the inner zone of the Emeishan LIP. The red and blue sticks in **g** indicate the splitting measurements in this article and a recent shear-wave splitting analysis[47], respectively; unfilled circles indicate the null measurements. Due to the undulation of the Moho depth, we apply different colour scales in **d** to denote the magnitude of crustal and mantle S-wave velocity at depth of 50 km. Red lines (AA', and BB') in **b** indicate the locations of cross-sections shown in Fig. 3.

135 km, which is isolated from the surroundings by the maximum gradient of velocity perturbations (Fig. 4).

Obvious HVA is also observed in the lithosphere beneath the Sichuan Basin (Fig. 2e–h). To further distinguish the properties of these HVAs, we perform SKS-wave splitting analysis along two orthogonal profiles (AA' and BB' shown in Fig. 2b) across the INZ, IMZ and OTZ (see "Methods" section for details). Shear-wave splitting measurements, shown in Supplementary Fig. 6, depict strong anisotropy beneath stations in the Sichuan Basin, in contrast to the weak anisotropy that appears at stations beneath the INZ. Especially, the core of INZ hosting the HVA in the lithospheric mantle is characterized by null or very weak splitting with delay times δt less than 0.35 s in nearly N-S-oriented fast directions (Figs. 2g and 3b, c, f, g). Conversely, strong N-S-oriented anisotropic zones with an average δt of 0.73 s appear to the west and north of the INZ; Nearly E-W-oriented anisotropy with an average δt of 0.74 s can be observed in the IMZ, and this orientation gradually shifts to NW-SE direction with an average δt of 0.87 s in the OTZ. The splitting features illustrate the contrasting natures of the HVAs in and out of the INZ (Figs. 2e–h).

Discussion

A magma plumbing system fossilized in a LIP

Our 3-D seismic image shows a translithospheric HVA with varying geometry and magnitude in depths, which could depict a complete view of the magmatism of the Emeishan LIP. The HVA in the crust beneath the INZ (sectors A, B, C in Fig. 4) is generally associated with high velocity, high resistance, and high Vp/Vs ratio detected by a series of 2-D geophysical investigations[30–32]. Those geophysical characteristics have well identified the underplating or magma reservoir at the base of the crust (sector C in Fig. 4) and intrusions within the crust (sectors A and B in Fig. 4) of the Permian plume. We thus interpret the crustal HVA as the magma plumbing system in the crust. Because little is known about the magmatism of the Emeishan LIP below the Moho depth, our discussion here will focus on the origin of the HVA in the subcontinental lithospheric mantle (SCLM) (sectors D, E in Fig. 4).

The HVA in the SCLM beneath the INZ features a vertical cylinder (Fig. 3d, h; sector E in Fig. 4), which is generally associated with a high-density anomaly reported by a previous gravity investigation[33]. The HVA is

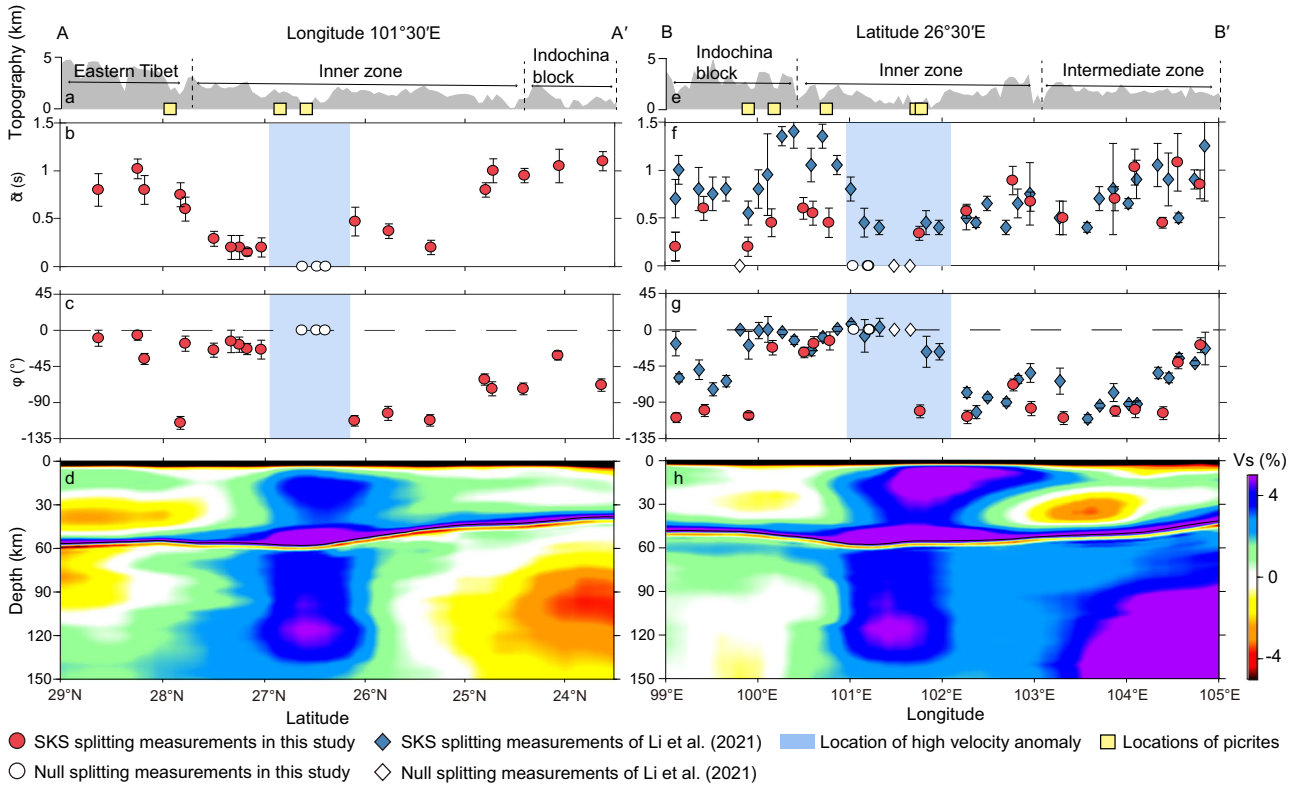

Fig. 3 | Seismic images of cross section and corresponding splitting analysis. **a**–**d** North-south cross-section at 101.5°E. **e**–**h** East-west cross-section at 26.5°N. Yellow squares in **a**, **e** indicate the localities of the picrites. Red circles and blue rhombuses in (**b**, **c**) and (**f**, **g**) represent the splitting measurements in this article and a recent shear-wave splitting analysis[47], respectively, while the unfilled circles and rhombuses indicate the null measurements. Colour scale of seismic images (**d**, **h**) denotes the percentage deviation from the average velocity (except for stations in the Sichuan Basin). Short bars represent the uncertainties of splitting measurements, and blue shades denote the areas with high-velocity anomaly in the subcontinental lithospheric mantle.

located at the center of the INZ and its size (with a diameter of ~100–125 km) is comparable with the expected size of a plume tail[34]. It is thus logically inferred that the HVA is above the plume axis[35]. Given an ancient LIP where thermal effects decayed out[11], the present temperature of its plumbing system should be similar to the ambient mantle. Thereby thermal anomaly is unlikely to be the cause of the HVA within the INZ, nor is grain size which leads to little discrepancies in seismic velocity with small temperature anomaly[36]. Most likely, the HVA in the SCLM is due to a compositional difference between it and the ambient mantle, for which two end-member models could be conceived: (1) depletion of the SCLM following extensive melt extraction[37,38]; (2) crystallization of the primary magma from the deep mantle[39]. In the first model, the HVA is mainly composed of remnant mineral assemblages of the SCLM after extensive melt extraction induced by the interaction between the mantle plume and the overlying lithosphere[37]. However, experimental data with pyrolite samples indicate that, when pressure exceeds 2.7 GPa, the predominant constituent of the SCLM (peridotite) changes only slightly with progressive melting[40]. In garnet stability field (>3 GPa), seismic velocities of residual harzburgite transformed from lherzolite by extensive partial melting are also indistinguishable from those of ambient SCLM[41]. Therefore, the comprehensive effect on the host uppermost mantle would not cause a notable HVA. Moreover, a reduction in the bulk density of the depleted mantle is expected in the melt extraction model[42], which is inconsistent with the observed high-density anomalies[30,33]. For the second model, the primary magma of the Emeishan LIP is suggested to be picrites containing 16–22 wt.% MgO[9,38,43]. A rock of picritic composition could be produced by rising magma in the plume tail due to the notable temperature difference (>200 °C) between the plume head and the SCLM[34,35]. Its high density at mantle pressures best explains both the present HVA and the positive gravity anomaly above the plume axis. On the other hand, geodynamic simulations suggested that the upwelling magmas directly impacted by the plume head could form a vertical crystalline lattice orientation of mantle minerals[44]. Then the crystallized products of the primary magma and its metamorphic phase (olivine-bearing eclogite) generate a continuous crystal framework, which can largely increase the seismic velocity[45]. We thus attribute the HVA in the SCLM primarily to the crystallization of primary magmas with vertical deforming fabrics, which is caused by the vertical migration of primary magmas from the deep mantle. A similar interpretation has also been applied to the HVA in the upper mantle beneath the Siberian LIP[46].

This interpretation is further supported by the strong spatial consistency of the HVA in the SCLM beneath the INZ with the weak or null splitting zone (Fig. 3). These results align well with the SKS-wave splitting measurements along a nearby E-W-trending linear seismic array[47] (Figs. 2g, 3f, g), where the optimal depth of the anisotropic layer is estimated to be between 100 and 200 km. We attribute this correlation to the fact that the anisotropy induced by the vertically oriented crystalline lattice of the primary magmas is undetectable by the steeply propagating SKS waves.

A much wider lateral extent of the magma storage system of the Emeishan LIP was inferred by radial anisotropy[48] extending to the HVA beneath the Sichuan Basin. By joint inversion of surface wave dispersions and receiver functions based on the dense array, our model is of a lateral resolution of about 30 km and therefore is capable of isolating the cylinder-shaped HVA beneath the INZ from the strong HVA at depths of 75–150 km close to the Sichuan Basin (Fig. 3h). We interpret the HVA close to the Sichuan Basin as the craton's keel rather than the fossilized root of the Emeishan LIP due to the strong SKS-wave splittings (Fig. 3g, Supplementary Fig. 6) as well as the absence of high-density anomalies[33] and picrite distribution in this region[12] (Fig. 1a).

Furthermore, to determine whether the Emeishan lavas were derived from a relatively homogeneous source or heterogeneous sources, we

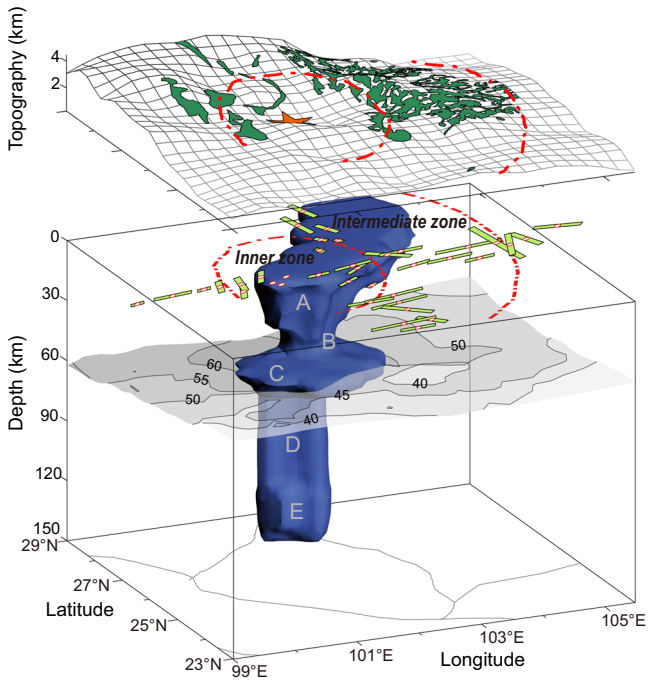

Fig. 4 | Three-dimensional visualization of the magma plumbing system of the Emeishan LIP shaped by the maximum gradient of velocity perturbations. The blue quasi-cylinder depicts the magma plumbing system. Grid lines indicate the surface undulations. The gray plane indicates the Moho discontinuity. The orange star corresponds to the location, where the core of the lower part (100–125 km) of the cylinder-shaped high-velocity anomaly is projected to the surface, and it is logically inferred as the plume center. The green areas indicate the distribution of the Permian basalts, the chartreuse bars indicate the SKS splitting measurements in this article shown in Fig. 2g, and the red dashed lines indicate the borders of the inner and intermediate zones of the Emeishan LIP. A, B, C, D, E indicate the different sectors of a high-velocity anomaly with varying geometry and magnitude.

combine constraints from our seismic model and geochemical observations. We note that the seismic velocities of the fossil magma conduit beneath the INZ decrease with depth from 100 km to 60 km (Fig. 3d, h; sector D in Fig. 4), which could be explained by decreasing degrees of magma melting and the entrainment of surrounding materials[34,49]. This gentle decrease suggests that there is no obvious compositional distinction within the magma storage system of the Emeishan LIP in the SCLM. In addition, the compositional diversity of the low-, intermediate- and high-Ti picrites can be used to evaluate the source of this LIP[5,50,51]. Their similar isotope compositions and trace element patterns[50], together with the relatively constant Pb isotope compositions of the Dali melt inclusions[13], reflect various degrees of melting of a relatively homogeneous source. Therefore, we suggest that the Permian mantle plume rose rapidly in the SCLM without undergoing largely cooling and fractionation.

The link between plate tectonics and LIPs

Although the fossilized Emeishan magma's plumbing system does not exhibit a complex network of channels in our seismic model, they are clearly distinguished from the surrounding host rock by a nearly-vertical quasi-cylinder-shaped HVA beneath the INZ (Fig. 4). It is widely postulated that the arrival of a plume head at the base of the lithosphere serves as a crucial driving force behind such a lithospheric plumbing system[4,34,35], and plume material migration beneath the lithosphere is mainly controlled by the plate motion[49,52]. To further comprehend the relationship between the vertical HVA and plate tectonics, investigating the interactions between the mantle plume and an overlying lithosphere is essential in the context of various plate velocities. We develop a 3-D numerical model (using CitcomCU software, see "Methods" section for details), along with incompressible fluids and a Boussinesq approximation[53], to investigate the evolution processes of the Emeishan LIP (Supplementary Fig. 7). The modeling result with a slow plate motion velocity (1 cm yr^{-1}) depicts a near-vertical ascent of the mantle plume with melt being concentrated within 300 km of the plume axis after ~7 Myr (Supplementary Fig. 7a, b). In contrast, when the plate motion rate increases to 6 cm yr^{-1}, the fast-moving plate causes deflection of the plume materials beneath the lithosphere, and the melt extends approximately 800 km from the plume axis in the direction of plate motion after the same period (Supplementary Fig. 7c, d). Overall, our geodynamic models identify that the temperature of the plume head is higher in a more concentrated manner with a higher melting extent when the overlying lithosphere has a slow motion. Its higher thermal buoyancy flux promotes the small-scale convection at the top of the plume, allowing locally for the thinning of the overlying lithosphere and subsequent emplacement of the magma[34,54]. That is indeed consistent with the interactions between the Emeishan plume and the overlying Yangtze craton: the lower part of the HVAs rooted in the SCLM beneath the INZ (sectors D, E in Fig. 4), which is logically above the plume axis, exhibits a perfectly vertical cylinder shape with a diameter of around 125 km. This consistency is also supported by the occurrence of picrites in the INZ[12,43] (Fig. 1a), which result from the high-temperature difference between the mantle plume and surrounding mantle and are most abundant towards the hot center of the plume head[34,35].

It is worth noting that the extension to the northeast of the upper part of the HVA (Figs. 2a, 3h; sector A in Fig. 4) rooted in the shallow crust does not indicate a fast plate motion as predicted by our geodynamic model. This extension could be controlled by the structure of the shallow crust, such as the pre-existing faults into the upper crust, along which massive flood basalts would have erupted and been buried in the Sichuan Basin[55]. The absence of low-Ti flood basalts and picrites in and around the Sichuan Basin indicates (Fig. 1a) that the temperature associated with the Permian plume in the OTZ is much lower than that in the INZ[56]. It also argues against the extension of the magma plumbing system to the northeast as predicted by our geodynamic model with high plate motion velocities (Supplementary Fig. 7c, d).

To further investigate whether the influence of slow plate motion velocity on the emplacement of magma, as proposed for the Emeishan LIP in this study, is a common mechanism for other LIPs, we extract local plate velocities within the main phases of the LIPs based on different kinematic plate reconstructions[57–59] using Gplates software (Supplementary Fig. 8). Except for ~10 cm $year^{-1}$ for the Deccan LIP, which is mainly affected by the collision between the Indian Plate and the Eurasian Plate, the average plate velocities in different plate reconstruction models for other LIPs are all less than 5 cm $year^{-1}$. Especially, near-zero plate velocities are coincident with the main window of magma emplacements of the Emeishan, Karoo-Ferrar, Parana-Etendeka, North-Atlantic and Columbia River LIPs. Notably, recent numerical modeling[52] and temporally resolved plate tectonic models[60] also identify that a slow plate motion rate plays a key role in the formations of LIPs. These temporal consistencies between the slow local plate motion and duration of main phases of LIPs from ~285 Ma to ~16 Ma indicate that the plate movements in the millions of years during magma emplacements are generally small throughout much of Earth's history, which may promote the emplacement of magma.

Thus, we conclude that, in addition to the arrival of the plume head, the overlying plate motions also play dominant roles in the magma emplacements of continental flood basalts and magmatic architectures of LIPs. The nearly static overlying plate provides enough time for the interactions between the mantle plume and the lithosphere, resulting in higher magma buoyancy fluxes, which makes the plume more effective in intruding the overlying plate and forming a LIP[34,54]. Conversely, considerable relative motion between the overlying tectonic plate and the deep mantle plume reduces the interaction time between the plume head and lithosphere, and accelerates the migration of plume materials beneath the lithosphere toward the plate motion direction. It could result in an elongated stripe structure with high seismic velocity in the lithosphere after the melt cools down. These fundamental relationships between mantle plumes and global plate tectonic processes may shed a light on investigating the roles of plumes in Earth's processes.

Methods

Ambient noise tomography

The dispersion curves for shorter periods (5–40 s) are provided by a seismic model of China on a 0.5° × 0.5° grid[25,26]. Rayleigh wave phase measurements in this model are obtained from the symmetric component of each inter-station cross-correlation by performing an automatic frequency time analysis[61,62], which is computed from several networks located throughout China and surrounding regions. Barmin's traditional ray theoretic method[63] is applied to generate isotropic phase velocity maps at each period. Damping and regularization are used to optimize the agreement between the maps. Eikonal method[64] is applied to estimate the spatial average of the uncertainties over the study area in this work.

Wave gradiometry method

We apply wave gradiometry method[22–24] to the seismograms for each event with the following procedures: (1) the mean, trend and instrument responses are removed from the raw waveforms; then narrow bandpass filters are applied to the displacement waveforms for 12 passbands with center periods ranging from 20 s to 150 s. (2) the maximum normalized cross-correlations between a test waveform and the signal at all other stations are calculated, and the test trace could be retained when more than half of the normalized cross-correlation values are better than 0.6. (3) the root mean square (rms) values of signal window and noise windows for each waveform are calculated. Signal window is defined by the signals between $t_{\mathrm{pick}} - 2\tau_{\max}$ and $t_{\mathrm{pick}} + 2\tau_{\max}$, where t_{pick} represents the timing of the waveform peak around the predicted group arrival time, $\tau_{\max}$ represents the maximum value of the period band of interest. Two noise windows are defined as the signals between the zero-lag time and the beginning of the signal window, and the part following the end of the signal window and with a delay of $4\tau_{\max}$ in time. We require that the ratio of these two rms values is greater than 3. (4) the methods of reducing velocity[23] and weighted inversion[24] are applied for irregular arrays. (5) spatial gradients of wavefield are obtained. (6) phase velocities are obtained by solutions linked with eikonal equation[24] at short periods (20 ~ 50 s), and those with Helmholtz equation[65] at longer periods (50 ~ 150 s), respectively.

Calculation of the receiver function

Time-domain iterative deconvolution technique is employed to each seismogram windowed between 20 s before and 30 s after the direct P wave arrival to calculate the radial receiver functions at stations[27,28]. In extracting the receiver functions, a low-pass Gaussian filter with a width of 2.5 s (pulse width of ~1 s) is applied to clean up the high-frequency noise. We carry out the moveout correction for Ps converted phases of each receiver function to a reference slowness of 0.06 s deg^{-1}. We use the receiver functions only within 9 s following the direct P-wave signal so that the waveforms include Ps phases converted at the Moho (Pms) but exclude the reverberated phases, on account of the distorted time and amplitude after the converted-phase moveout correction for the latter. Following three criteria are applied to choose the reliable receiver functions: (1) the variance reduction in the iterative deconvolution is greater than 80%; (2) the amplitude of the receiver function at the zero time is between 0 and 1; and (3) the misfit of receiver function is less than 0.08. We then use the harmonic stripping method[29] to compute the azimuthally independent receiver function from all the quality-controlled receiver functions (Supplementary Fig. 9). Only if more than 10 individual receiver functions from different earthquakes at a station pass the quality control, these receiver functions are stacked to obtain the average receiver function of each station and used in the joint inversion. Ultimately, we obtain average receiver functions with a high signal-to-noise ratio for 420 stations.

Joint inverting for shear wave velocity

A Bayesian Monte Carlo approach for joint inversion of dispersion curves and average receiver functions is employed in this study[29]. By combining the two complementary data types, it provides information about well-constrained absolute lithospheric shear wave velocity and sharp seismic discontinuities beneath the seismic station (Supplementary Fig. 10). We parameterize the 3-D shear wave velocity model of the study area as a combination of a set of 1-D depth-dependent models at each station[29], which is composed of a sedimentary layer, a crustal layer, and an uppermost mantle layer. In detail, the sedimentary layer is parameterized with linear gradient velocities defined by the layer thickness and velocities at the top and bottom of the layer; the crustal and mantle layers are characterized by four and five cubic B-splines, respectively; and the crust thickness is also a free parameter during the inversion. The Vp/Vs ratio is set as 2.0 in the sedimentary layer, and 1.75 in the crustal and mantle layers. Density is calculated as a simple approximation from the empirical relationships in the sedimentary and crustal layers[66], and the mantle[67], respectively. To make physical dispersion correction, an attenuation factor Q taken from the PREM model[68] is used in the inversion. Prior distribution of models in the joint inversion is defined by allowed perturbations relative to the reference model as well as model constraints. In this study, the reference model is derived from the AK135 model[69] and the following two constraints are imposed on the model space: (1) Vs increases with depth across the model discontinuities at the base of the sediments and Moho; (2) Vs does not exceed 4.9 km s^{-1} at all depths.

The principal output of the joint inversion is the posterior distribution of models, which is conducted through forward computation using the Thomson-Haskell method with an earth-flattening transformation[29]. During model space sampling, each model is generated by perturbing a given model under the prior assumptions and the Metropolis law[29] is utilized as the transition probability. Furthermore, a joint misfit function as follows is introduced as the basis for accepting models to form the posterior distribution:

$$S(\boldsymbol{m}) = S_{\mathrm{SW}} + \frac{1}{\kappa} S_{\mathrm{RF}} = \sum_{i=1}^{N} \frac{\left[g_i(\boldsymbol{m}) - D_i^{\mathrm{obs}}\right]^2}{\sigma_i^2} + \frac{1}{\kappa} \sum_{j=1}^{M} \frac{\left[R_j(\boldsymbol{m}) - A_0\left(t_j\right)\right]^2}{s_j^2} \quad (1)$$

Where $g_i(\boldsymbol{m})$ and D_i^{obs} denote the predicted (from the model $\boldsymbol{m}$) and the observed phase velocities at period i on a discrete grid of N periods. $R_j(\boldsymbol{m})$ and $A_0(t_j)$ denote the predicted (from the model $\boldsymbol{m}$) and observed receiver functions at time t_j on a discrete grid of M times. The coefficient κ represents the weight between the dispersion data and the receiver function. Because both the data sets are equally reliable in this study, we set κ as 2.5 to strike the appropriate balance between the two data sets[29]. σ is the uncertainty of Rayleigh wave dispersion curves, which is estimated by the eikonal method[64]. S_j represents the uncertainty of the receiver function, which is computed by the harmonic stripping method[29]. The choice of critical threshold of the misfit is described by Shen et al.[29]. Finally, an average of 20,000 accepted models are retained in the posterior distribution for each station in order to enhance the reliability of the results.

SKS-waves splitting analysis

To perform an SKS-wave splitting analysis along the profiles AA' and BB' in Fig. 2b, SKS-waves from 186 events at epicentral distances of 85°−130°with the earthquake magnitude larger than Mw 5.5 (Supplementary Fig. 2) are used through the SplitLab software package[70]. Considering its steeper incident angles and higher signal-to-noise ratio[30], we choose only SKS-waves to ensure a high lateral resolution. After the waveforms are band-pass filtered between 0.04–0.5 Hz, the rotation cross-correlation method[71] and the eigenvalue method[72] are applied simultaneously to determine the fast polarization direction and the delay time, and only unambiguous measurements with Signal-to-noise ratio ≥ 4.0 are selected. We present the splitting measurements from the eigenvalue method in this study, while the difference in fast wave direction, Δφ, and the ratio of delay time, ρ, between measurements of different methods are evaluated simultaneously to determine the quality of the measurements[73]. We only choose the splitting

measurements with $0.7 \le \rho \le 1.2$ and $\Delta\varphi \le 15°$, and null (non-splitting) measurements with $\rho \le 0.25$ and $35° \le \Delta\varphi \le 55°$. The average splitting for each station is calculated by stacking the normalized energy maps of reliable splitting measurements, and a statistical F test is conducted to obtain the 95% confidence interval[72] to estimate the corresponding uncertainty. The station-averaged splitting results are shown in Supplemental Table 1. Azimuthal dependence of the splitting parameters is observed at several stations in the IMZ and OTZ of the Emeishan LIP, which suggests that multiple layers of seismic anisotropy may exist over there. We therefore focus on the cause of weak or null and strong splitting measurements in and out of the INZ in this study. Moreover, we find little consistency between our measurements and crustal anisotropies constructed by Pms splitting analysis[74] (Supplementary Fig. 11), indicating a mantle source for the SKS splitting measurements in this study.

Geodynamic modeling

The governing equations are the same as those in Zhong[53]. Our model domain ranges from 0 km to 4800 km in the X direction with 256 elements, from 0 km to 2400 km in the Y direction with 128 elements, and from 0 km to 600 km in depth (Z direction) with 64 elements. Considering that the Emeishan LIP was located at the margin of the Yangtze Craton during its magma emplacement, we set the thickness of the overlying plate as 100 km. The linear initial temperature within the lithosphere is applied in our geodynamic model with a potential temperature of 1400 °C. The nondimensional viscosity depends on temperature and depth, consistent with previous studies[52,75].

In addition, isothermal boundary conditions are prescribed at the top and bottom boundaries in our model, while the other boundary conditions are thermally insulated. Mechanically, all the sides are free-slip except that the left ($X = 0$ km), right ($X = 4800$ km) and bottom boundaries are permeable. Initially, a semicircular thermal anomaly with an excess temperature of 300 K and a radius of 100 km is located at ($X = 1600$ km, $Y = 0$ km). The distribution of excess temperature in the anomalous area is given by $\triangle T = \triangle T_{\mathrm{p}} \exp\left(\frac{-r^2}{R^2}\right)$, where R is the plume radius, and r is the horizontal distance from the plume center. To investigate the interactions between the mantle plume and the moving lithosphere, the lithosphere starts moving at a rate of 1 or 6 cm yr^{-1} when the plume rises to a depth of ~250 km. We defined this time as 0 Myr. Besides, the extent of anhydrous melting is estimated based on a parameterization method[76].

Data availability

Waveform data of permanent stations for this study are collected through Data Management Centre of China National Seismic Network at Institute of Geophysics, China Earthquake Administration (https://doi.org/10.11998/SeisDmc/SN, http://www.seisdmc.ac.cn). Waveform data of portable stations are archived at China Seismic Array Data Management Centre at Institute of Geophysics, China Earthquake Administration (https://doi.org/10.12001/ChinArray.Data, http://www.chinarraydmc.cn). Geospatial Data is available in https://github.com/gmt-china/china-geospatial-data. Surface wave dispersion curves, velocity model of Vsv, and original receiver functions are available in the figshare (https://doi.org/10.6084/m9.figshare.24025494).

Code availability

The wave gradiometry code is available at https://github.com/Feihuang-C/Wave-Gradiometry. The receiver function analysis code can be found at http://eqseis.geosc.psu.edu/cammon/HTML/RftnDocs/rftn01.html. The Computer Programs in Seismology (CPS, version 3.30) software package can be accessed at http://www.eas.slu.edu/eqc/eqccps.html. The code of forward computation is available at http://www.eas.slu.edu/eqc/eqccps.html. The code of SplitLab software package is available at http://www.gm.univ-montp2.fr/splitting/. The mantle convection code CitcomCU is available at https://geodynamics.org/cig/. The Gplates software (version 2.5) can be accessed at https://www.earthbyte.org/download-gplates-2-5/. Figures in this study were generated using GMT[77].

Received: 20 September 2023; Accepted: 16 August 2024;
Published online: 26 August 2024

References

1. Cashman, K. V., Sparks, R. S. J. & Blundy, J. D. Vertically extensive and unstable magmatic systems: a unified view of igneous processes. *Science* **355**, eaag3055 (2017).
2. Campbell, I. H. & Kerr, A. C. The great plume debate: testing the plume theory. *Chem. Geol.* **241**, 149–152 (2007).
3. Coffin, M. F. & Eldholm, O. Large igneous provinces-crustal structure, dimensions, and external consequences. *Rev. Geophys.* **32**, 1–36 (1994).
4. Xu, Y.-G., He, B., Chung, S. L., Menzies, M. A. & Frey, F. A. Geologic, geochemical, and geophysical consequences of plume involvement in the Emeishan flood-basalt province. *Geology* **32**, 917–920 (2004).
5. Xu, Y.-G. & He, B. Thick, high-velocity crust in the Emeishan large igneous province, southwestern China: Evidence for crustal growth by magmatic underplating or intraplating. In *Plates, Plumes and Planetary Processes* (eds Gillian, R. F. & Donna, M. J.) 841–858 (GSA, 2007).
6. Morgan, W. J. Convection plumes in the lower mantle. *Nature* **230**, 42–43 (1971).
7. Cammarano, F., Goes, S., Vacher, P. & Giardini, D. Inferring upper-mantle temperatures from seismic velocities. *Phys. Earth Planet. Inter.* **138**, 197–222 (2003).
8. Hawkesworth, C., Cawood, P. & Dhuime, B. Continental growth and the crustal record. *Tectonophysics* **609**, 651–660 (2013).
9. Chung, S. & Jahn, B. Plume-lithosphere interaction in generation of the Emeishan flood basalts at the Permian-Triassic boundary. *Geology* **23**, 889–892 (1995).
10. He, B., Xu, Y.-G., Chung, S. L., Xiao, L. & Wang, Y. Sedimentary evidence for a rapid, kilometer-scale crustal doming prior to the eruption of the Emeishan flood basalts. *Earth Planet. Sci. Lett.* **213**, 391–405 (2003).
11. Shellnutt, J. G. & Jahn, B.-M. Origin of Late Permian Emeishan basaltic rocks from the Panxi region (SW China): implications for the Ti-classification and spatial–compositional distribution of the Emeishan flood basalts. *J. Volcanol. Geotherm. Res.* **199**, 85–95 (2011).
12. Hanski, E., Kamenetsky, V. S., Luo, Z.-Y., Xu, Y.-G. & Kuzmin, D. V. Primitive magmas in the Emeishan large igneous province, southwestern China and northern Vietnam. *Lithos* **119**, 75–90 (2010).
13. Ren, Z. Y. et al. Primary magmas and mantle sources of Emeishan basalts constrained from major element, trace element and Pb isotope compositions of olivine-hosted melt inclusions. *Geochim. Cosmochim. Acta* **208**, 63–85 (2017).
14. Fan, W., Zhang, C., Wang, Y., Guo, F. & Peng, T. Geochronology and geochemistry of Permian basalts in western Guangxi Province, Southwest China: evidence for plume-lithosphere interaction. *Lithos* **102**, 218–236 (2008).
15. Huang, H. et al. Eruptive tempo of Emeishan large igneous province, southwestern China and northern Vietnam: relations to biotic crises and paleoclimate changes around the Guadalupian-Lopingian boundary. *Geology* **50**, 1083–1087 (2022).
16. Zhong, Y. T., He, B., Mundil, R. & Xu, Y.-G. CA-TIMS zircon U-Pb dating of felsic ignimbrite from the Binchuan section: implications for the termination age of Emeishan large igneous province. *Lithos* **204**, 14–19 (2014).
17. Ridley, V. A. & Richards, M. A. Deep crustal structure beneath large igneous provinces and the petrologic evolution of flood basalts. *Geochem. Geophys. Geosyst.* **11**, Q09006 (2010).
18. Thybo, H. & Artemieva, I. M. Moho and magmatic underplating in continental lithosphere. *Tectonophysics* **609**, 605–619 (2013).
19. Black, B. A., Karlstrom, L. & Mather, T. A. The life cycle of large igneous provinces. *Nat. Rev. Earth Environ.* **2**, 840–857 (2021).

20. Ding, Z. & Wu, Z. Advances of ChinArray program. In *Proceedings of the American Geophysical Union, Fall Meeting 2013*, S54A-01. https://ui.adsabs.harvard.edu/abs/2013AGUFM.S54A..01D (2013).
21. Zheng, X. F., Yao, Z. X., Liang, J. H. & Zheng, J. The role played and opportunities provided by IGP DMC of China National Seismic Network in Wenchuan earthquake disaster relief and researches. *Bull. Seismol. Soc. Am.* **100**, 2866–2872 (2010).
22. Langston, C. A. Wave gradiometry in the time domain. *Bull. Seismol. Soc. Am.* **97**, 926–933 (2007).
23. Langston, C. A. Wave gradiometry in two dimensions. *Bull. Seismol. Soc. Am.* **97**, 401–416 (2007).
24. Liang, C. & Langston, C. A. Wave gradiometry for USArray: Rayleigh waves. *J. Geophys. Res.: Solid Earth* **114**, B02308 (2009).
25. Shen, W. et al. A seismic reference model for the crust and uppermost mantle beneath China from surface wave dispersion. *Geophys. J. Int.* **206**, 954–979 (2016).
26. Shen, W. et al. China/Tibet Surface Wave Dispersion Maps. http://ciei.colorado.edu/DispMaps (2015).
27. Ammon, C. J. The isolation of receiver effects from teleseismic P waveforms. *Bull. Seismol. Soc. Am.* **81**, 2504–2510 (1991).
28. Ligorría, J. P. & Ammon, C. J. Iterative deconvolution and receiver-function estimation. *Bull. Seismol. Soc. Am.* **89**, 1395–1400 (1999).
29. Shen, W., Ritzwoller, M. H., Schulte-Pelkum, V. & Lin, F.-C. Joint inversion of surface wave dispersion and receiver functions: a Bayesian Monte-Carlo approach. *Geophys. J. Int.* **192**, 807–836 (2013).
30. Chen, Y. et al. Magmatic underplating and crustal growth in the Emeishan Large Igneous Province, SW China, revealed by a passive seismic experiment. *Earth Planet. Sci. Lett.* **432**, 103–1114 (2015).
31. Li, X. et al. A plume-modified lithospheric barrier to the southeastward flow of partially molten Tibetan crust inferred from magnetotelluric data. *Earth Planet. Sci. Lett.* **548**, 116493 (2020).
32. Liang, X., Wang, Q., Chen, Y. & Hung, S.-H. Possible residuary lithospheric signature of Permian Emeishan plume from multiscale body-wave finite frequency tomography. In *Proceedings of the American Geophysical Union, Fall Meeting 2018*, T51D-0194. https://ui.adsabs.harvard.edu/abs/2018AGUFM.T51D0194L (2018).
33. Deng, Y. et al. Mantle origin of the Emeishan large igneous province (South China) from the analysis of residual gravity anomalies. *Lithos* **204**, 4–13 (2014).
34. Griffiths, R. W. & Campbell, I. H. On the dynamics of long-lived plume conduits in the convecting mantle. *Earth Planet. Sci. Lett.* **103**, 214–227 (1991).
35. Campbell, I. H. Large igneous provinces and the mantle plume hypothesis. *Elements* **5**, 265–269 (2005).
36. Dannberg, J. et al. The importance of grain size to mantle dynamics and seismological observations. *Geochem. Geophys. Geosyst.* **18**, 3034–3061 (2017).
37. Xu, J., Suzuki, K., Xu, Y.-G., Mei, H. & Li, J. Os, P. B., and Nd isotope geochemistry of the Permian Emeishan continental flood basalts: insights into the source of a large igneous province. *Geochim. Cosmochim. Acta* **71**, 2104–2119 (2007).
38. Xu, Y.-G. et al. Origin of two differentiation trends in the Emeishan flood basalts. *Chin. Sci. Bull.* **48**, 390–394 (2003).
39. Liu, J., Liu, F., He, J., Chen, H. & You, Q. The tomographic research of Pan Xi ancient rifting-conclusion inferred from the structure and the evolution of the crust-mantle. *Sci. China Ser. D: Earth Sci.* **30**, 9–15 (2000).
40. Takahashi, E. Melting of a dry peridotite KLB-1 up to 14 GPa: Implications on the origin of peridotitic upper mantle. *J. Geophys. Res.: Solid Earth* **91**, 9367–9382 (1986).
41. Matsukage, K. N., Nishihara, Y. & Karato, S. Seismological signature of chemical differentiation of Earth's upper mantle. *J. Geophys. Res.* **110**, B12305 (2005).
42. Afonso, J. C. & Schutt, D. L. The effects of polybaric partial melting on density and seismic velocities of mantle restites. *Lithos* **134-135**, 289–303 (2012).
43. Zhang, Z., Mahoney, J. J., Mao, J. & Wang, F. Geochemistry of picritic and associated basalt flows of the western Emeishan flood basalt province, China. *J. Petrol.* **47**, 1997–2019 (2006).
44. Ito, G. et al. Seismic anisotropy and shear wave splitting associated with mantle plume-plate interaction. *J. Geophys. Res.: Solid Earth* **119**, 4923–4937 (2014).
45. Caricchi, L., Burlini, L. & Ulmer, P. Propagation of P and S-waves in magmas with different crystal contents: insights into the crystallinity of magmatic reservoirs. *J. Volcanol. Geotherm. Res.* **178**, 740–750 (2008).
46. Bascou, J. et al. Seismic velocities, anisotropy and deformation in Siberian cratonic mantle: EBSD data on xenoliths from the Udachnaya kimberlite. *Earth Planet. Sci. Lett.* **304**, 71–84 (2011).
47. Li, W., Chen, Y., Liang, X. & Xu, Y. G. Lateral seismic anisotropy variations record interaction between Tibetan mantle flow and plume-strengthened Yangtze Craton. *J. Geophys. Res.: Solid Earth* **126**, e2020JB020841 (2021).
48. Liu, Y., Li, L., van Wijk, J., Li, A. & Fu, Y. V. Surface-wave tomography of the Emeishan large igneous province (China): Magma storage system, hidden hotspot track, and its impact on the Capitanian mass extinction. *Geology* **49**, 1032–1037 (2021).
49. Griffiths, R. W. & Campbell, I. H. Stirring and structure in mantle starting plumes. *Earth Planet. Sci. Lett.* **99**, 66–78 (1990).
50. Kamenetsky, V. S., Chung, S., Kamenetsky, M. B. & Kuzmin, D. V. Picrites from the Emeishan large igneous province, SW China: a compositional continuum in primitive magmas and their respective mantle sources. *J. Petrol.* **53**, 2095–2113 (2012).
51. Xiao, L. et al. Distinct mantle sources of low-Ti and high-Ti basalts from the western Emeishan large igneous province, SW China: implications for plume–lithosphere interaction. *Earth Planet. Sci. Lett.* **228**, 525–546 (2004).
52. Liu, H. & Leng, W. Tarim large igneous province caused by a wide and wet mantle plume. *J. Geophys. Res.: Solid Earth* **125**, e2019JB019001 (2020).
53. Zhong, S. Constraints on thermochemical convection of the mantle from plume heat flux, plume excess temperature, and upper mantle temperature. *J. Geophys. Res.: Solid Earth* **111**, B04409 (2006).
54. Griffiths, R. W. & Campbell, I. H. Interaction of mantle plume heads with the Earth's surface and onset of small-scale convection. *J. Geophys. Res.: Solid Earth* **96**, 18295–18310 (1991).
55. He, L. Emeishan mantle plume and its potential impact on the Sichuan Basin: insights from numerical modeling. *Phys. Earth Planet. Inter.* **323**, 106841 (2022).
56. Meng, F. et al. Geochemistry and petrogenesis of Late Permian basalts from the Sichuan Basin, SW China: implications for the geodynamics of the Emeishan mantle plume. *J. Asian Earth Sci.* **241**, 105477 (2023).
57. Young, A. et al. Global kinematics of tectonic plates and subduction zones since the late Paleozoic Era. *Geosci. Front.* **10**, 989–1013 (2019).
58. Merdith, A. S. et al. Extending full-plate tectonic models into deep time: linking the Neoproterozoic and the Phanerozoic. *Earth-Sci. Rev.* **214**, 103477 (2021).
59. Müller, R. D. et al. A tectonic-rules based mantle reference frame since 1 billion years ago–implications for supercontinent cycles and plate-mantle system evolution. *Solid Earth* **13**, 1127–1159 (2022).
60. Ruhl, M. et al. Reduced plate motion controlled timing of Early Jurassic Karoo-Ferrar large igneous province volcanism. *Sci. Adv.* **8**, eabo0866 (2022).
61. Bensen, G. D. et al. Processing seismic ambient noise data to obtain reliable broad-band surface wave dispersion measurements. *Geophys. J. Int.* **169**, 1239–1260 (2007).
62. Lin, F.-C., Moschetti, M. P. & Ritzwoller, M. H. Surface wave tomography of the western United States from ambient seismic noise:

Rayleigh and Love wave phase velocity maps. *Geophys. J. Int.* **173**, 281–298 (2008).
63. Barmin, M. P., Ritzwoller, M. H. & Levshin, A. L. A fast and reliable method for surface wave tomography. *Pure Appl. Geophys.* **158**, 1351–1375 (2001).
64. Lin, F.-C., Ritzwoller, M. H. & Snieder, R. Eikonal tomography: surface wave tomography by phase front tracking across a regional broad-band seismic array. *Geophys. J. Int.* **177**, 1091–1110 (2009).
65. Liu, Y. & Holt, W. E. Wave gradiometry and its link with Helmholtz equation solutions applied to USArray in the eastern U.S. *J. Geophys. Res.: Solid Earth* **120**, 5717–5746 (2015).
66. Christensen, N. I. & Mooney, W. D. Seismic velocity structure and composition of the continental crust: a global view. *J. Geophys. Res.: Atmos.* **100**, 9761–9788 (1995).
67. Karato, S. & Wu, P. Rheology of the upper mantle: a synthesis. *Science* **260**, 771–778 (1993).
68. Dziewonski, A. & Anderson, D. Preliminary reference earth model. *Phys. Earth Planet. Inter.* **25**, 297–356 (1981).
69. Kennett, B. L. N., Engdahl, E. R. & Buland, R. Constraints on seismic velocities in the earth from travel-times. *Geophys. J. Int.* **122**, 108–124 (1995).
70. Wüstefeld, A., Bokelmann, G., Zaroli, C. & Barruol, G. SplitLab: a shear-wave splitting environment in Matlab. *Comput. Geosci.* **34**, 515–528 (2008).
71. Bowman, J. R. & Ando, M. Shear-wave splitting in the uppermantle wedge above the Tonga subduction zone. *Geophys. J. Int.* **88**, 25–41 (1987).
72. Silver, P. G. & Chan, W. W. Shear-wave splitting and subcontinental mantle deformation. *J. Geophys. Res.: Solid Earth* **96**, 16429–16454 (1991).
73. Wüstefeld, A. & Bokelmann, G. Null detection in shear-wave splitting measurements. *Bull. Seismol. Soc. Am.* **97**, 1204–1211 (2007).
74. Zeng, S. et al. Crustal structure and anisotropy measured by CHINArray and implications for complicated deformation mechanisms beneath the eastern Tibetan margin. *J. Geophys. Res.: Solid Earth* **129**, e2023JB028332 (2024).
75. Liu, H., Chen, F., Leng, W., Zhang, H. & Xu, Y.-G. Crustal footprint of the Hainan plume beneath southeast China. *J. Geophys. Res.: Solid Earth* **123**, 3065–3079 (2018).
76. Katz, R. F., Spiegelman, M. & Langmuir, C. H. A new parameterization of hydrous mantle melting. *Geochem. Geophys. Geosyst.* **4**, 1073 (2003).
77. Wessel, P. et al. The generic mapping tools version 6. Geochem. *Geochem. Geophys. Geosyst.* **20**, 5556–5564 (2019).

Acknowledgements

The work was funded by National Key R&D Program of China (grant 2022YFF0802600), NSFC (grants 42274082, 42030108, and 42204096), the United Laboratory of High-Pressure Physics and Earthquake Science (grant 2022HPPES06), the MOST Special Fund from State Key Laboratory of Geological Processes and Mineral Resources (MSFGPMR2024-502), and the Distinguished Young Scientist Team Funds for the Central Universities, China University of Geosciences (Wuhan) (grant 106-G1323523051), and the "CUG Scholar" Scientific Research Funds at China University of Geosciences (Wuhan) (grant 2022111). Generic Mapping Tools (GMT) (Wessel and Smith, 1996) are used to plot figures.

Author contributions

S.W. in interaction with Y.Z. and Y.C. collected and processed the seismic data. H.L. carried out the geodynamic modeling. S.A., S.Z., L.Q., and R.G. also contributed to the data collection. S.W., Y.Z., Y.C., and H.L. wrote the original draft. X.Y. and Y.X. developed the initial interpretation. All authors contributed to writing of the paper.

Competing interests

The authors declare no competing interests.

Additional information

Supplementary information The online version contains supplementary material available at https://doi.org/10.1038/s43247-024-01631-0.

Correspondence and requests for materials should be addressed to Yong Zheng or Yun Chen.

Peer review information *Communications Earth & Environment* thanks the anonymous reviewers for their contribution to the peer review of this work. Primary Handling Editors: Lucia Pappalardo and Joe Aslin. A peer review file is available.